

Chlorine tailored p-d blocks dual-metal atomic catalyst for efficient photocatalytic CO₂ reduction

Hainan Shi ^a, Jiahui Li ^a, Haozhi Wang ^b, Jungang Hou ^{a,*}, Keyan Li ^{a,*}, Xinwen Guo ^{a,*}

^a State Key Laboratory of Fine Chemicals, Frontier Science Center for Smart Materials, School of Chemical Engineering, Dalian University of Technology, Dalian 116024, China

^b State Key Laboratory of Marine Resource Utilization in South China Sea, School of Materials Science and Engineering, Hainan University, Haikou 570228, China



ARTICLE INFO

Keywords:

Atomically dispersed catalysts
p-d blocks dual-metal sites
Chlorine atom tailored
CO₂ photoreduction

ABSTRACT

Solar-driven CO₂ conversion into solar fuels has attracted much attention, but suffers from the low catalytic efficiency. Herein, we reports an In based dual-metal atomically dispersed photocatalyst consisting of Cl tailored p-d blocks active sites anchored on carbon nitride nanosheets. The CO₂ photoreduction on CuInCN exhibits an excellent CO production rate of 1.2 mmol g⁻¹ h⁻¹, nearly ten times higher than that on CN. Combined experimental investigation with DFT calculation, this work reveals that d-block Cu metal introduced into InCN enhances the light absorption, electronic conductivity, and charge separation, as the same time, provides the abundant active sites. Subsequently, Cl atom in the structure further promotes the charge separation and electron mobility, modulates the electronic structure of Cu-In to make them synergistically interact via In-N-Cu configuration, greatly lowering the energy barrier of *COOH formation. Consequently, these make CuInCN act an effective photocatalyst for CO₂ conversion.

1. Introduction

Solar-driven CO₂ conversion to chemical feedstocks is a promising solution to balance the carbon-recycling and utilizes renewable energy [1–4]. Carbon monoxide (CO) is one of important C₁ product, serving as the basic reagent hydrogenation to form industrial chemicals and fuels [5–8]. Unfortunately, the fast photoinduced charge recombination and the lack of surface active sites limit the further improvement of the photocatalytic performance. This puts forward high requirements upon photocatalysts design for CO₂ reduction reaction (CO₂RR).

Among various catalysts, single atom catalysts (SACs) have shown the great advantages in heterogeneous catalysis [9–15], especially for photocatalytic CO₂RR [16–21]. This is because SACs possessed almost 100% atomic utilization can provide the efficient surficial active sites compared with the traditional metal nanoparticles. Atomic modification also offers an opportunity to accelerate the charge transfer from bulk to surface of catalysts. Moreover, the isolate metal atom with the unique unsaturated coordination environment has a flexible electronic structure to activate the catalysts [22,23]. More importantly, the electronic configuration of isolated metal atom can be modulated by introducing another component or manufacturing vacancy [24,25]. Thus, an atomic p-block metal catalyst may afford a solution to enhance the performance

of CO₂ photoreduction to CO by modulating its electronic property to make it more efficient in activating the catalyst or intermediate.

The p-block metal of indium (In) SAC has gained great interesting in electrocatalytic CO₂RR [25–28]. The products are concentrated in CO and HCOOH. For example, In SAC containing exclusive isolated In-N₄ atomic interface sites were reported to support CO₂ electroreduction to formic acid with TOF of 12,500 h⁻¹ and faradaic efficiency (FE) of 96% [26]. Another atomic In catalyst anchored on N doped carbon (In_x/NC) was shown to exhibit outstanding electrocatalytic CO₂ to CO production with TOF of 40,000 h⁻¹ and FE of 97.2% [28]. Especially, In-N₃-V with vacancy transformed from In-N₄ configuration greatly enhanced CO TOF with 27 times higher. Because the vacancy changed the electronic structure of In site, lowering the activation energy [25]. To sum up, In SAC is a promising candidate for CO₂RR. Fine modulating of the electronic structure of In atom can boost the catalytic performance. Nevertheless, as far as we know, few efforts about In SACs were studied for photocatalytic CO₂RR. In addition, a catalyst possessing multiple functionalities would be better met the multiple demands for CO₂RR to achieve high photocatalytic performance. Especially, it is essential to regulate the moderate adsorption strength of key intermediate on dual-atom sites, and a synergistic effect and electron redistribution between bimetal sites [29–33]. Inspired of these advantages, the

* Corresponding authors.

E-mail addresses: jhou@dlut.edu.cn (J. Hou), keyanli@dlut.edu.cn (K. Li), guoxw@dlut.edu.cn (X. Guo).

emergence of dual-atom/metal atomic catalysts have become a promising strategy to optimize the catalytic performance.

Taking into consideration of above, atomically dispersed p-d blocks In based dual-metal catalysts have been developed for photocatalytic CO₂ to CO. The aim is to regulate the electronic structure of In active sites by introduction of d-block metal. By examining the precursor of d-block metals, the photocatalytic performance and reaction mechanism were investigated. Herein, a family of atomically dispersed p-d blocks In-based dual-metal anchored on a polymeric carbon nitride (CN) was prepared by using a facile thermal polymerization strategy for photocatalytic CO₂RR. Combined extensive experimental investigation with DFT calculation, the mechanism of CO₂ photoreduction was unveiled by elucidating the light absorption, charge dynamics, electronic structure of metal active sites, coupling the activation energy barrier, and adsorption of key *COOH intermediate on metal sites to underpin the high performance of the catalyst.

2. Experimental

2.1. Preparation of photocatalysts

Carbon nitride (CN): 10 g urea was put into the 100 mL crucible and calcinated at 550 °C for 3 h with 5 °C/min rate. The light yellow powder was obtained and denoted as CN.

Dual metal catalysts: Cu-In dual-metal catalyst was synthesized through a facile thermal polymerization method. Taking CuInCN (0.34% Cu + 1.2% In) for example, briefly, 1.5 mL of CuCl₂ aqueous (2.66 mg/mL) was dissolved in 25 mL ethanol, then 10 g urea was added. The mixture was heated at 90 °C for 1 h and further dried at 60 °C under vacuum. The obtained powder mixed with 12 mg of MIL-68 was ground for 30 min to form a homogeneous phase. They were put into the 100 mL crucible then sealed by tinfoil. Then the mixture was calcinated at 550 °C for 3 h at 5 °C/min rate. The obtained sample was denoted as CuInCN.

10 g urea mixed with a certain of MIL-68(In) and Cu₃(BTC)₂ was ground for 30 min to form a homogeneous phase. The next step was the same as CuInCN. The obtained sample was denoted as CuInCN-M. The Cu loading measured by ICP was controlled as similar to CuInCN.

Other In-based dual-metal catalysts were prepared as the similar procedure to that of CuInCN except CuCl₂ replaced by other metal chlorides.

The synthesis of CuCN and InCN was followed the similar procedure to that of CuInCN without adding MIL-68 and CuCl₂, respectively.

2.2. Photocatalytic CO₂ RR

Photocatalytic CO₂RR was conducted in a quartz vessel (46 mL) at 25 °C by circulation cooling system and at atmosphere pressure. Light source was a 300 W Xenon lamp equipped with a cut-off filter ($\lambda > 420$ nm) (CEL-HXF300-T3, Beijing China Education Au-light Co., Ltd., China). Typically, 3 mg catalyst was dispersed in a 6 mL solvent of MeCN: TEOA: H₂O (v/v = 4:1:1), containing 20 mmol/L bpy in MeCN solvent, and 100 μL of CoCl₂ aq (5 mmol/L). The above mixture was ultrasonic for 20 min, and then purified by CO₂ (99.999%) for 20 min to remove air. Finally, the photocatalytic reactor was sealed. The products were detected by a syringe at 1 h intervals with the gas Chromatograph (GC-2014, Shimadzu) equipped with FID detector connection with methane reforming furnace and TCD detector (5 A molecular sieve column). Ar was used as a carrier gas. The evolution rate (R) and selectivity (Sel.) of product was calculated by the following equations, respectively.

$$R = C_i * \left(\frac{PV}{RT} \right) / (M_c * t) * 10^6 \quad (1)$$

$$\text{Sel.} = \frac{m_p \times N_e}{m_{CO} \times 2 + m_{H_2} \times 2} * 100\% \quad (2)$$

where R represents the evolution rate of product (μmol g⁻¹ h⁻¹), C_i (ppm) is the mole concentration obtained by GC, P represents the pressure of reaction (Pa), V is the volume of reactor (m³), R is 8.314, T denotes the temperature of 298 K, M_c represents the mass of catalyst (g), t represents the reaction time (h), m_p represents mole of product (umol), N_e represents the number of electrons.

3. Results and discussion

3.1. Structure analysis

Fig. 1 shows the preparation, morphology structure results of as-prepared In single atom catalyst (InCN) and atomically dispersed p-d blocks Cu-In active sites modulated by Cl atom (CuInCN). **Fig. 1a** illustrates the two paths of thermal polymerization procedure employed in producing InCN (path 1) and CuInCN (path 2). The precursors were subjected to heat treatment during which polymerization of urea occurred resulting into the formation of atomically dispersed In and Cu atoms supported on carbon nitride (CN). For comparison purposes, its Cu SAC counterparts was also prepared in this study (the sample prepared with CuCl₂ is represented by CuCN without special explanation).

Scanning electron microscopy (SEM) and transmission electron microscopy (TEM) images of MIL-68 (In) show a nanorod shape (**Fig. S1, Supporting Information**), while InCN displays a microstructure consisting of randomly arranged nanosheets, similar to the morphologies of pure CN, but smaller size with obviously porous structure (**Fig. S2**). CuInCN displays the more curly nanosheets compared with InCN. **Figs. 1b** and **S3** present the aberration-corrected high-angle annular dark-field scanning TEM (AC-HAADF-STEM) images of InCN, revealing the well dispersed and isolated spots throughout the nanosheets. X-ray spectroscopy (EDS) shows the uniform distributed C, N, In elements in InCN. These results indicate that InCN consists of atomic In supported on CN. Also, isolated Cu atoms on CN are observed in CuCN (**Fig. S4**). Compared with InCN, uniformly dispersed isolated spots with high density are observed in CuInCN (**Fig. 1c**). Especially, when further zoned in **Fig. S5a,b**, it reveals some paired of atoms with bright and dark spots, which are identified as In (bright) and Cu (dark) atoms, respectively. This observation indicates that as-prepared CuInCN consists of atomic In and Cu atoms anchored on CN nanosheets, with some distinctively paired In-Cu configurations. EDS further confirms the existence of In and Cu distributed homogeneously. Importantly, the presence of Cl element is also observed in CuInCN (**Figs. 1d** and **S5c-e**).

Powder X-ray diffraction (XRD) patterns of the catalysts are shown in **Fig. S6**. Two typical diffraction peaks at 13.1 and 27.2° correspond to (100) and (002) plane of CN with regards to in-plane ordered stacking and interlayered stacking of the conjugated tri-s-triazine structure, respectively. For InCN, no obvious structure changes compared with pure CN, but crystallinity reduces with increased In loading (**Fig. S6a**). Note that the peaks assigned to In₂O₃ are observed when InCN was calcinated at 450 °C (**Fig. S6b**), indicating the structure of In species in InCN is totally different from In₂O₃. Moreover, the introduction of Cu atoms into InCN still remains the structure of CN whether CuCl₂ or Cu-MOF was used as precursor (**Fig. S6c,d**). Fourier transform infrared spectroscopy (FTIR) of the catalysts as shown in **Fig. S7** also verify the above results of metal-loading unchange the structure of CN. X-ray photoelectron spectroscopy (XPS) further determined the chemical state of catalysts as shown in **Figs. S8 and S9**. As seen, N 1 s XPS of InCN and CuCN shift to the lower binding energy compared with that of CN, signifying the presence of metal–N bonding which leads to increased electron cloud density of N environment. However, the shift of the binding energy in N 1 s XPS of CuInCN is not obvious, suggesting that Cu and In atoms have opposite effects on N element. For In 3d XPS spectra of InCN, the peaks at 445.7 and 453.1 eV correspond to In³⁺ 3d_{5/2} and In³⁺ 3d_{3/2}. The binding energy of peaks in CuInCN shifts to 0.1 eV lower, manifesting an increase of electron density at In sites relative to that of

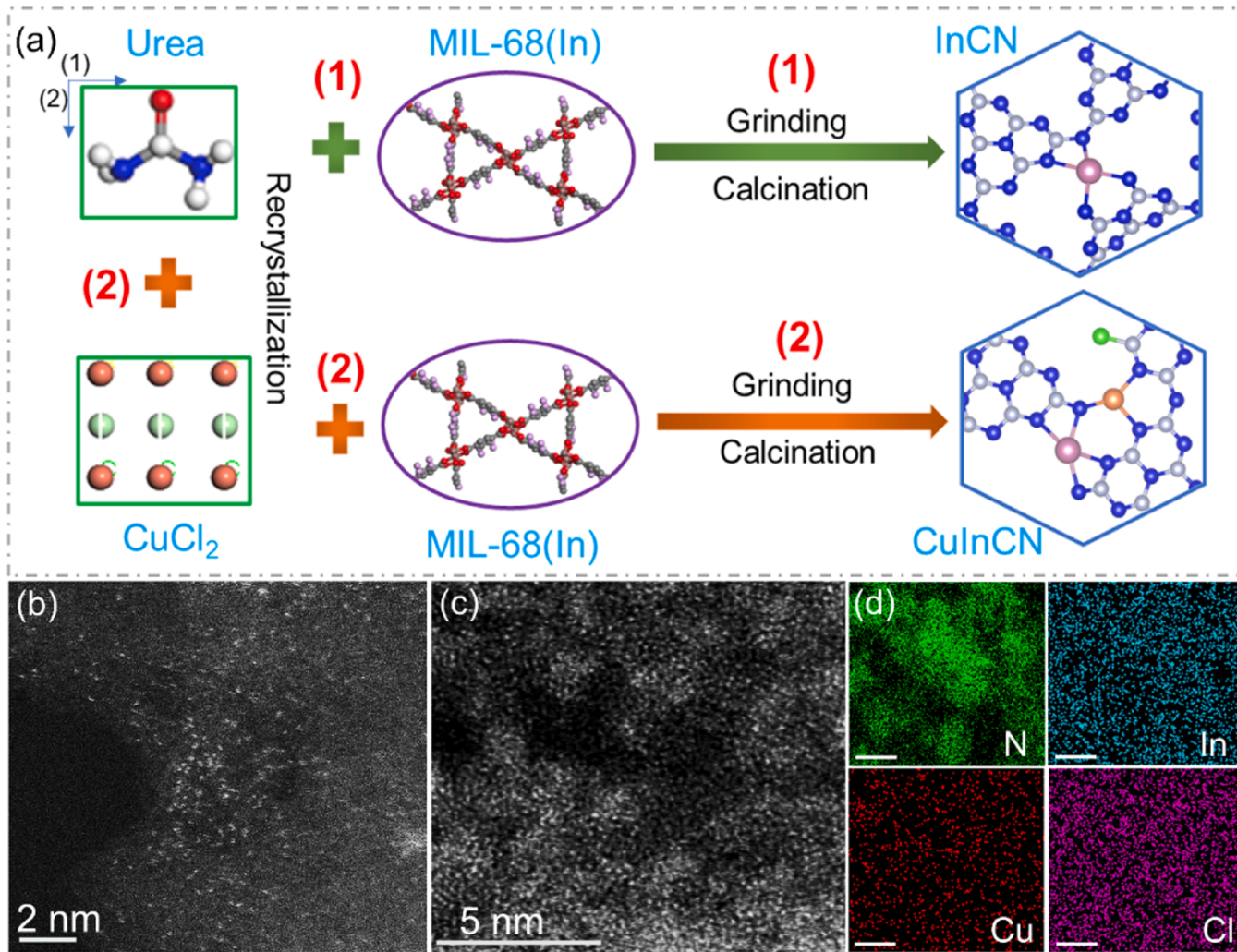


Fig. 1. Schematic diagram of prepared process for InCN and CuInCN (light gray: C atom, blue: N atom, red: O atom, white: H atom, pale purple: In atom, orange: Cu atom, green: Cl atom) (a), AC-HAADF-STEM images of InCN (b), CuInCN (c), element mapping for CuInCN, scale bar: 2 μm (d).

InCN. For Cu 2p XPS of CuCN and CuInCN, no satellite peaks are observed compared with CuO. At the same time, the binding energy of peaks located around 932.4 and 952.1 eV are much lower than that in CuO (933.6 and 953.6 eV). These observations suggest that Cu species in CuInCN and CuCN mainly exist the Cu⁺/Cu⁰. Importantly, Cl 2p XPS signal were also detected on CuCN and CuInCN. The peak at 197.9 eV assigned to Cu–Cl or C–Cl bond, demonstrating that Cl is also present in the structure of CuInCN and CuCN.

Fig. 2 presents the results of X-ray absorption fine structure (XAFS) to further ensure the coordination environments and local structure of CuInCN. As shown in Fig. 2a, In K-edge X-ray absorption near-edge structure (XANES) curves of CuInCN was analyzed with In foil and In₂O₃ as references. The near-edge absorption peak of CuInCN almost coincides with that of In₂O₃, indicating In species exist in In³⁺. Fig. 2b displays the Fourier-transformed extended X-ray absorption fine structure (EXAFS) spectra of samples. As seen, the *R* position of In-In bond in In foil and In₂O₃ are 2.97 and 3.09 Å (phase-uncorrected distance), whereas for In-O coordination, it is at ~1.72 in In₂O₃. Only a main peak at ~1.65 Å in the *R* space is observed in CuInCN. No In-In bond contributes in CuInCN, which is further testified by wavelet transform (WT) contour plots of In K-edge weighted EXAFS (Fig. 2g-i). Combining with HAADF-STEM results, it confirms the atomically dispersed In species in CuInCN. Fig. 2c show the fitting results of the *R* space, disclosing that each In atom coordinates with four N atoms of CN with the average In-N bond length of about 2.15 Å (Table S1).

Meanwhile, Fig. 2d shows the Cu *K*-edge XANES profiles of CuInCN as well as the references of Cu foil, Cu₂O, CuO and CuPC. The geometrical configuration of Cu sites is different from these references, and Cu species exist in Cu⁺ form in CuInCN. The phase-uncorrected EXAFS spectra present the *R* space position in the first shell at ~2.25 Å for Cu–Cu coordination of Cu foil, 1.46 and 1.54 Å for Cu–O bond of Cu₂O and CuO, respectively, 1.47 Å for Cu–N scattering of CuPC and CuInCN (Fig. 2e). Because CuInCN shows a symmetric peak at ~1.47 Å, which is not consistent with asymmetric Cu–Cl scattering at ~1.8 Å in *R* space position [34]. Thus, no Cu–Cl coordination is formed in the first scattering in CuInCN. However, according to the Cl element detected in XPS spectra and EDS, it is possible for Cl to coordinate to C atom of CN. A weak peak at ~2.37 Å is also observed in CuInCN, which can be contributed to the scattering between Cu atoms and C/N. WT results combined with O 1 s XPS give further support that Cu atom only exhibits Cu–N coordination environment distinguished from Cu–Cu bond (Fig. 2j-l), proving the atomically dispersed Cu species on CN. The best-fitting analysis the extended Cu *K*-edge clearly determines that one Cu center is coordinated with three N atoms of tri-s-triazine units in CN with bond length of 1.90 Å in the first scattering path (Fig. 2f and Table S2). The coordination configuration for CuInCN was further investigated by quantitative EXAFS curve fitting analysis (Fig. S10). According to the XAFS results, the optimized model of In and Cu structure in CuInCN by density functional theory (DFT) determines that In–N₄ and Cu–N₃ configuration connected by In–N–Cu bridge in first

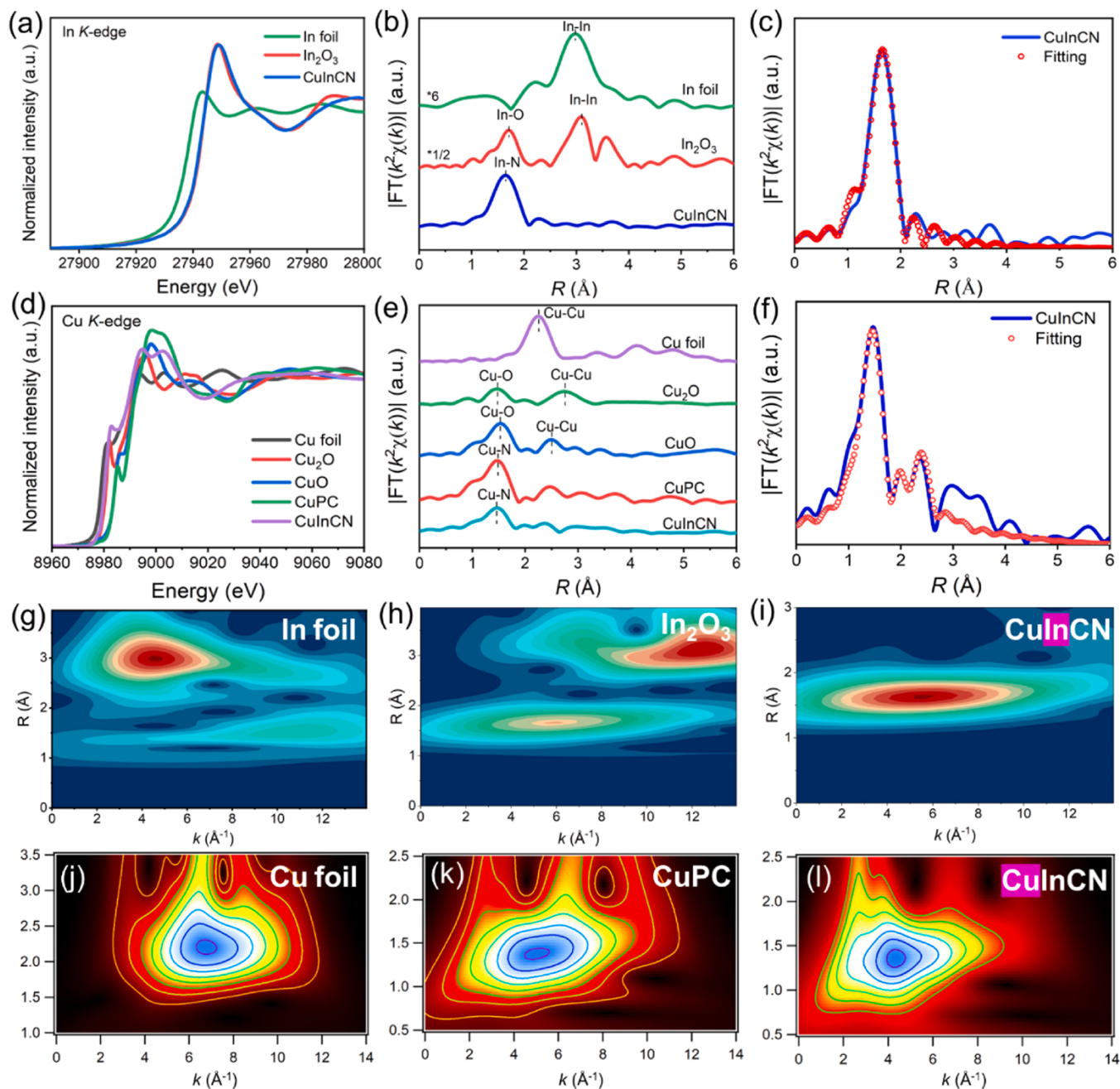


Fig. 2. CuInCN at In K-edge: Normalized XANES (a), Fourier transform EXAFS spectra (b), EXAFS curves fitting in R space (c). CuInCN at Cu K-edge: Normalized XANES (d), Fourier transform XAFS spectra (e), EXAFS curves fitting in R space (f). Wavelet transform contour plots of CuInCN at In K-edge: In foil (g), In₂O₃ (h), CuInCN (i). CuInCN at Cu K-edge: Cu foil (j), CuPC (k), CuInCN (l).

scattering shell. The calculated bond length of 2.19 Å for In–N and 1.88 Å for Cu–N coordination well coincides with the EXAFS fitting results (In–N, 2.15 Å and Cu–N, 1.90 Å).

Based on the above analysis, it reveals that In and Cu species are atomically dispersed on CN nanosheets, with a fraction of In and Cu appearing in intimate atomic pairs. Specifically, In and Cu atoms are anchored on CN structure via the coordination of In–N₄ and Cu–N₃ connected by In–N–Cu bridges, and Cl atom nearby In–Cu configuration coordinates with C atom.

3.2. Photoreduction of CO₂

Considering the unique structure of CuInCN photocatalyst, the performance of photocatalytic CO₂RR in a hybrid photocatalytic system

was investigated. CO and H₂ were detected as the main products, with the trace of CH₄. No liquid products such as HCOOH, CH₃OH were detected. As shown in Figs. 3a and S11, InCN exhibits a remarkably enhanced CO evolution compared with CN. The yield and selectivity of CO firstly increase and then decrease with increased In loading. InCN with 1.2 wt% In content shows the maximum CO production rate (588.4 μmol g⁻¹ h⁻¹) and selectivity of 90.4%, five times higher than CN. The CO generation declines sharply when InCN after calcination transformed to In₂O₃/CN (Fig. 3b), indicating that In SACs show an overwhelming advantage. In comparison with other MOFs as precursors, the CO evolution on InCN is highest, demonstrating the outstanding behavior of In active species anchored on CN during photoreduction of CO₂RR (Fig. 3c). When d-block metal atoms were introduced in InCN, CuInCN exhibits the highest CO yield in comparison with FeInCN, CoInCN and

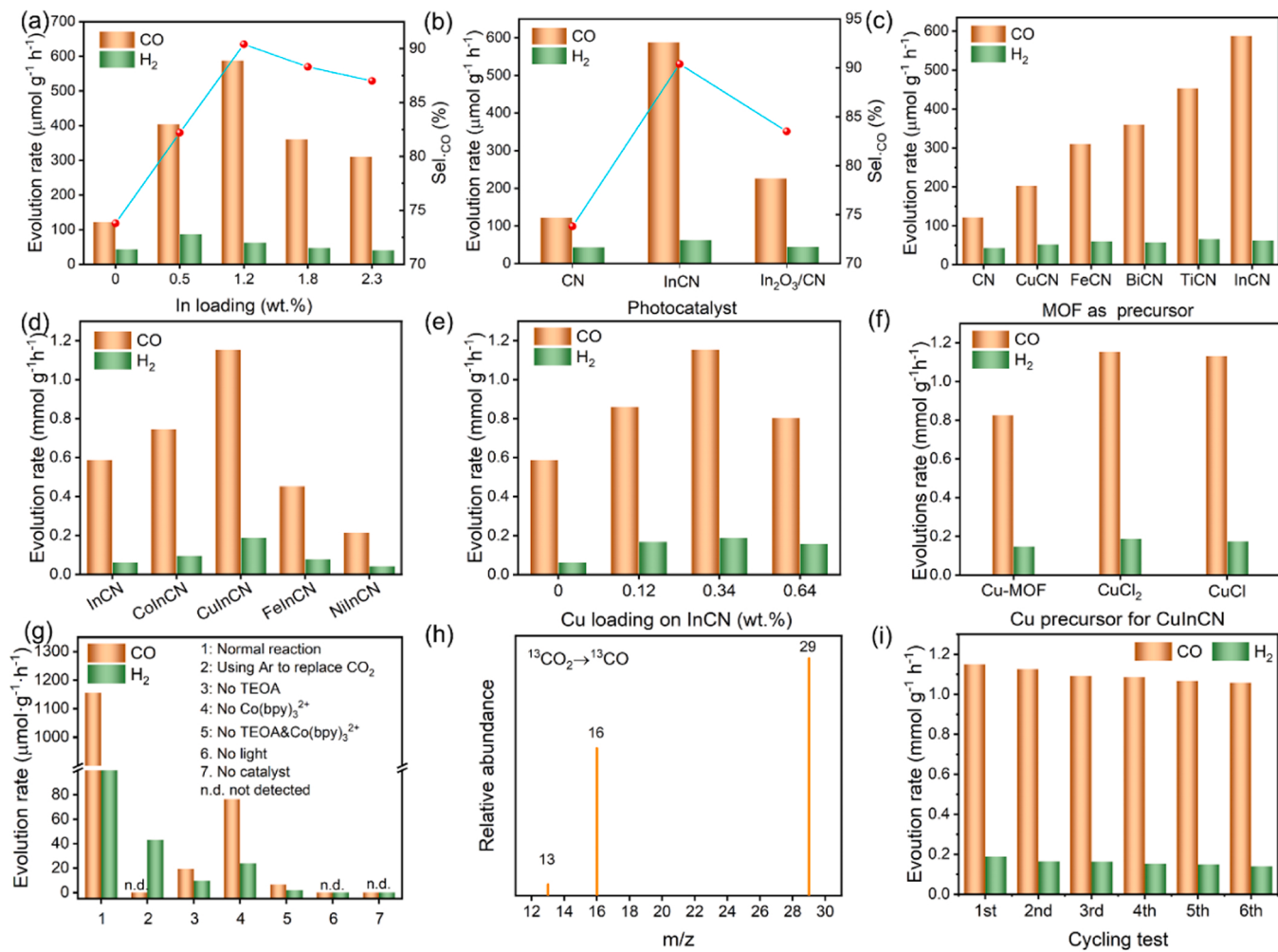


Fig. 3. Product evolution rate over InCN with different In loading (a), comparison of performance on InCN and In₂O₃/CN obtained from calcination of InCN (b), metal species on CN by using MOF as precursor with the same metal loading (c), performance comparison on different d-block metal introduced into InCN by using metal chloride as precursor (the same mass percent content of d-block metal) (d), the product distribution on CuInCN with different Cu loading into InCN (1.2 wt.%) (e), the performance comparison on CuInCN by using different Cu-based precursors (f), control experiment for photocatalytic CO₂RR (g), MS results of product by using ¹³CO₂ (h), cycling test of CuInCN (i). Reaction condition: 3 mg catalyst in 6 mL solvent, MeCN:H₂O:TEOA = 4:1:1, [Co(bpy)₃]²⁺ as cocatalyst, $\lambda > 420$ nm, T = 25 °C, reaction time of 3 h.

NiInCN, indicating the significantly intimate interaction between Cu and In atoms (Fig. 3d).

Fig. 3e shows the catalytic activity of CuInCN by controlling Cu loading. CuInCN with 0.34 wt% Cu loading exhibits the optimal CO evolution, reaching 1.2 mmol g⁻¹ h⁻¹, two times higher than that on InCN, and ten times higher relative to that on CN (Figs. S12 and S13). Fig. 3f presents the catalytic performance of CuInCN by using different Cu precursors, revealing that CuInCN using cuprous chloride as precursor exhibits the superior CO evolution, higher than that using Cu-MOF as precursors (denoted as CuInCN-M). This discloses that the unique CuInCN structure consisting of anion Cl is more favorable for photocatalytic CO₂RR to CO.

Fig. 3g presents the results of controlling experiments to investigate the effect of reaction conditions. As shown, the photocatalytic CO₂RR cannot be triggered without light irradiation or catalysts. Few products were detected without TEOA or [Co(bpy)₃]²⁺, which function as hole scavenging agent and cocatalyst, respectively. Only H₂ were generated as Ar replaced CO₂, suggesting that CO product can only be converted from CO₂, which was further confirmed by ¹³C isotope test (Fig. 3h). CuInCN not only exhibits the high photocatalytic activity towards CO₂ to CO, but also has a good catalytic stability as demonstrated in Fig. 3i. The CO evolution shows a slightly decrease after CuInCN subjected to six

photocatalytic cycles. And no obvious structure change is observed between the fresh and used catalysts from XRD and FTIR spectra (Fig. S14). In addition, the used CuInCN still displays the atomic dispersion of In and Cu sites and there is no agglomeration (Fig. S15).

3.3. Reaction mechanism

Based on above the catalytic performance results, a series of characterizations were carried out to explain the structure-performance relationship. Fig. 4 presents the CO₂ adsorption, light absorption, and charge separation of CuInCN and its counterparts. Firstly, N₂ adsorption-desorption isotherms of prepared catalysts show the typical IV-H₃ type hysteresis (Fig. S16), suggesting a mesoporous architecture. The obtained specific surface area and pore volume are listed in Table S3. Compared with CN (48.1 m² g⁻¹, 0.21 cm³ g⁻¹), the specific surface area and pore volume of InCN remarkably increase (89.2 m² g⁻¹, 0.63 cm³ g⁻¹). There is no obvious enlargement in CuCN (50.1 m² g⁻¹, 0.28 cm³ g⁻¹). However, Cu introduced into InCN (CuInCN) presents an increased surface area and pore volume (93.8 m² g⁻¹, 0.71 cm³ g⁻¹). There is a slight change for CuInCN by using CuCl₂ or Cu-MOF as precursor. Secondly, CO₂ uptakes of these samples as shown in Fig. 4a demonstrates that InCN exhibits an apparently increased CO₂ adsorption

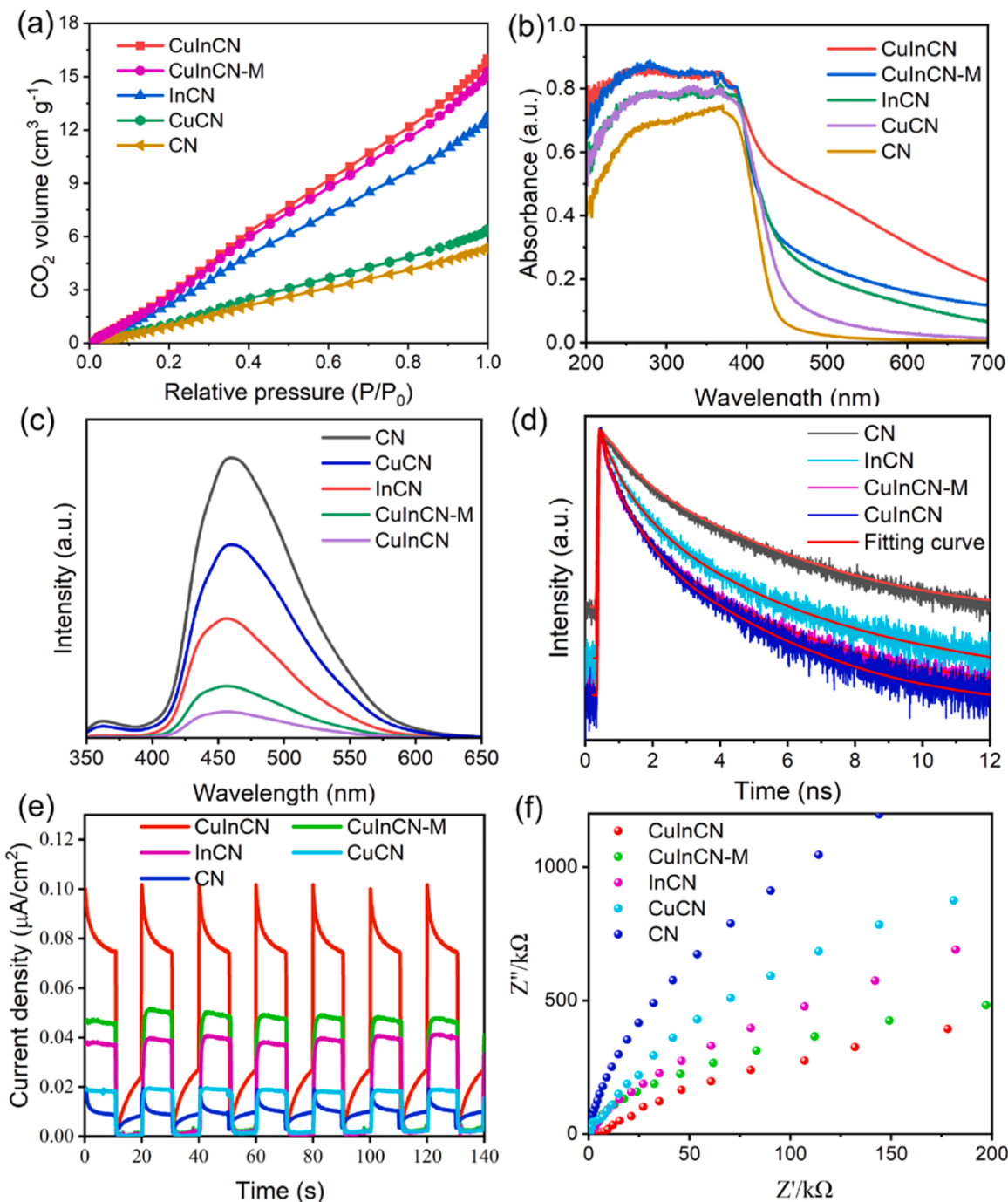


Fig. 4. CO₂ adsorption isotherms (a), UV-Vis absorption spectra (b), PL spectra (c), tr-PL spectra (d), photocurrent curves (e), EIS spectra (f) of prepared samples.

compared with CN. Notably, Cu introduced into InCN can further promote CO₂ adsorption although CuCN itself has a weak affinity to CO₂. CO₂ adsorption on CuInCN is slightly better than that on CuInCN-M. The above results indicate that p-d blocks In-Cu dual metal photocatalysts show an improving surface property good for CO₂ adsorption. Also CuInCN exhibits a good CO₂ adsorption superior to other In-based dual-metal catalysts (Fig. S17).

The results of UV-Vis diffuse reflection spectra (UV-Vis DRS) of prepared samples are presented in Fig. 4b, indicating that InCN show an obviously enhanced light absorption compared with CN and CuCN. Particularly, CuInCN displays a dramatically improved light absorption and narrowed band gap (E_g). The optics properties of CuInCN by using CuCl₂ as precursor is superior to that by using of Cu-MOF precursor. The

conduction band (CBM) of these materials determined by Mott-Schottky curves have barely changed (Fig. S18), which indicates that valence band (VBM) of catalysts becomes smaller according the narrowed band gap. Fig. 4c shows the steady photoluminescence (PL) spectra of samples. It reveals that In-Cu dual metal catalysts present a visibly enhanced fluorescence quenching signal compared with CN, InCN and CuCN, demonstrating that dual metal system is more favorable to inhibit the charge recombination. Moreover, CuInCN exhibits the lower PL intensity relative to that CuInCN-M, indicating that the anion Cl in the structure of CuInCN greatly promotes the charge separation.

Time-resolved PL (tr-PL) spectroscopy was performed to deeply investigate the charge separation mechanism as shown in Fig. 4d. Notably, the tr-PL spectra exhibit multi-exponential decay, and metal/

CN samples show a faster decay compared with CN. The fitting results including the lifetime (t_1), and amplitude (A_1) are provided in Table S4. CN contains two lifetimes (0.78 ns, 61% and 4.1 ns, 39%) assigned to radiative recombination. In contrast, for the metal/CN samples, the decay curves are best fitted with three lifetimes. An additional more shorter lifetime (0.15–0.2 ns) with approximate 50% amplitude are observed except two long-lived lifetimes. Consequently, the amplitudes of two longer lifetimes are much smaller compared to those of CN. The shortest lifetime is attributed to the electron transfer from CN to metal sites, which is the reason why metal/CN show the much stronger PL quenching than CN. Evidently, electron transfer can obviously improve the efficiency of charge separation. Compared to individual metal/CN, the shortest lifetimes of dual-metal catalysts are shorter and the amplitudes are larger than InCN, indicating that In-Cu dual-metal system is most efficient in supporting the charge transfer process from CN to metal to promote charge separation. In addition, CuInCN displays a longer long-lived lifetimes compared with CuInCN-M, suggesting that some defects caused by the presence of Cl in CuInCN functions as the trapped sites for electrons, which is favorable for photocatalytic reactions.

Photoelectrochemical tests of these catalysts were also executed to further explore the charge separation efficiency as depicted in Fig. 4e,f. Fig. 4e presents a sensitive photocurrent response of catalysts on/off visible-light irradiation cycles. Obviously, the photocurrent is CuInCN>CuInCN-M>InCN>CuCN>CN. Electrochemical impedance spectra (EIS) of these samples exhibit the arc radius of CuInCN<CuInCN-M<InCN<CuCN<CN. The above results of photo-electrochemical tests combined with steady and transient PL spectra reveal the following points underpinning the high performance. (i) The electron transportation in atomically dispersed single metal catalysts is faster than CN; (ii) In-Cu dual metal atomically dispersed catalysts are more beneficial to charge separation and electron transportation; (iii) Cl in CuInCN further promotes charge separation and transportation relative to that

without Cl.

The DFT calculation was performed to further unveil the reaction mechanism. Note that two CuInCN models were established in our work, one with Cl atom (named CuInCN) and another one without Cl atom (named CuInCN-M) provided in Fig. S19. Fig. 5 presents the density of states, work function, and charge density difference of the catalysts being studied.

Total density of states of InCN and CuInCN are shown in Fig. 5a,b, as well as CN provided in Fig. S20. CN displays a typical semiconductor characteristics. In contrast, no electrons are contributed around the Fermi level for InCN. However, a new electronic state appears between VBM and CBM. The electrons of In 5p and N 2p contribute the new electronic state, signifying In atom on CN changes the electronic structure of the coordinated N atoms. CuInCN displays the electronic density of state near the Fermi level. Note that the electrons of Cu 3d and N 2p contributes the most near Fermi level, disclosing that Cu atom introduced into InCN increase the electronic conductivity and provide the active sites. Fig. 5c presents the partial density of state of In 5p for the three catalysts. No electron appears near the Fermi level for InCN. In contrast, there are few electronic states in CuInCN-M, indicating that the introduction of Cu atom into InCN leads to In sites active. Moreover, more electronic states appear near the Fermi level as Cl atom exists in the structure of CuInCN, revealing that Cl atom further modulates the band structure of In sites making it more active.

The work function (Φ) of InCN and CuInCN are presented in Fig. 5c, d, while the work function of CN and CuInCN-M are displayed in Fig. S21. The work function can be estimated by the energy difference from Fermi level to vacuum level based on the electrostatic potential of a material [32,35]. The work function of InCN (5.93 eV) is higher than that of CN (4.50 eV), suggesting that electrons are prone to bind to In sites. The work function of CuInCN-M (6.54 eV) is higher than that of InCN, which indicates the stronger binding of In-Cu dual-metal to

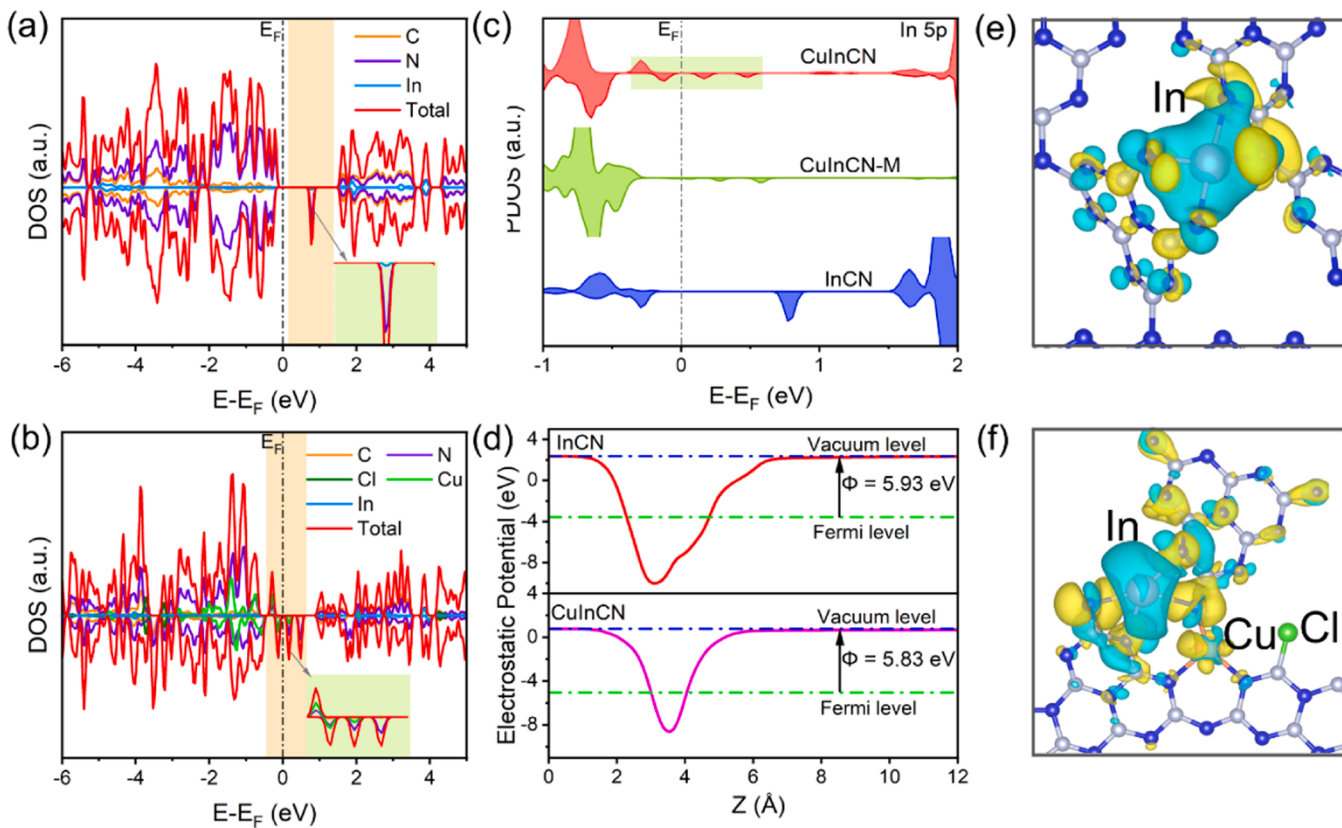


Fig. 5. Total density of state of InCN (a), CuInCN, (b) partial density of state of In 5p for CuInCN, CuInCN-M and InCN (c), work function of InCN and CuInCN (d), differential charge density of InCN (e) and CuInCN (f). (light gray: C atom, blue: N atom, pale purple: In atom, orange: Cu atom, green: Cl atom).

electrons [32]. However, CuInCN has the lower work function (5.83 eV) compared with InCN and CuInCN-M, demonstrating that Cl in the structure can mediate the binding strength of metal sites to electrons, facilitating charge mobility efficiently.

Fig. 5e,f present the differential charge density of InCN and CuInCN. For InCN, there is a strong charge depletion on In site (cyan isosurface) and an charge accumulation on N sites coordinated In atom (yellow isosurface), suggesting the central of In atom with much unoccupied *p* orbital. Clearly, the electron distribution of In-Cu configuration catalysts indicates less charge depletion to the catalyst surface on In site than that on the In site of InCN (Figs. 5f and S22). Compared the two structure of In-Cu catalyst with Cl and without Cl atom, it reveals that more charge depletion on In site at presence of Cl atom in In-Cu catalyst relative to that without Cl atom. The results unravel that the central of In site in CuInCN binds with O stronger than CuInCN-M, weaker than InCN [36]. Meanwhile, CuInCN in which Cl exists nearby In-Cu configuration exhibits a less electron accumulation than that without Cl on Cu site.

Based on above DFT results and analysis, it discloses that the introduction of d-block Cu atom increases the electronic conductivity, provides the active sites, regulates the band structure of In atom. And Cl atom nearby In-Cu configuration makes In sites more active, promotes the electron mobility, modulates the charge density of nearby In and Cu sites.

Electronic properties of catalysts are closely related to catalytic activity and affect the adsorption mode of key intermediates. The in-situ diffuse reflectance infrared Fourier-transform spectroscopy (DRIFTS) on CuInCN were obtained during CO₂ photoreduction reaction with

increased irradiation times as presented in Fig. S23. Note that the peaks at 1349 cm⁻¹, 1416 cm⁻¹ and 1682 cm⁻¹ are indexed to adsorbed *b*-CO₂²⁻, HCO₃⁻ and •CO₂, respectively [20,37]. Importantly, the peaks of 1651 cm⁻¹ is assigned to *COOH [20,32], which is the key intermediate for CO₂ reduction to CO. Based on the results of in-situ DRIFTS, DFT calculation further investigate the Gibbs free energy barrier of each elemental reaction. Fig. 6a illustrates the Gibbs free energy diagrams of CO₂ photoreduction on CuInCN, CuInCN-M and InCN, respectively. As seen, the formation of *COOH is rate-determining step on CuInCN and CuInCN-M. In contrast, the formation of *CO appears to be the rate-determining step on InCN and CuCN (Fig. S24).

On CuInCN and CuInCN-M, the formation of *COOH is endothermic. The energy barrier of *COOH formation on CuInCN ($\Delta G = + 0.79$ eV) is lower than that on CuInCN-M ($\Delta G = + 1.19$ eV). The *CO formation and desorption is downhill in free energy changes. By contrast, on InCN, the formation of *COOH is exothermal. The formation of *CO is endothermic, the energy barrier is 2.24 eV, much higher than that of the formation of *COOH on CuInCN with or without Cl, which is the reason that In-Cu dual metal catalysts are superior to InCN for CO₂ photoreduction. In addition, compared with other In based dual-metal catalysts, the formation of *COOH intermediate is also the rate-determining (Fig. S25). However, the energy barrier of *COOH formation on CuInCN is the lowest among other In based dual-metal catalysts. It also explains the better catalytic performance on CuInCN.

Fig. 6b presents the adsorption model and adsorption energy of *COOH on these three catalysts to further explain the Gibbs free energy difference. As shown, *COOH is adsorbed on In and Cu site by In-O and

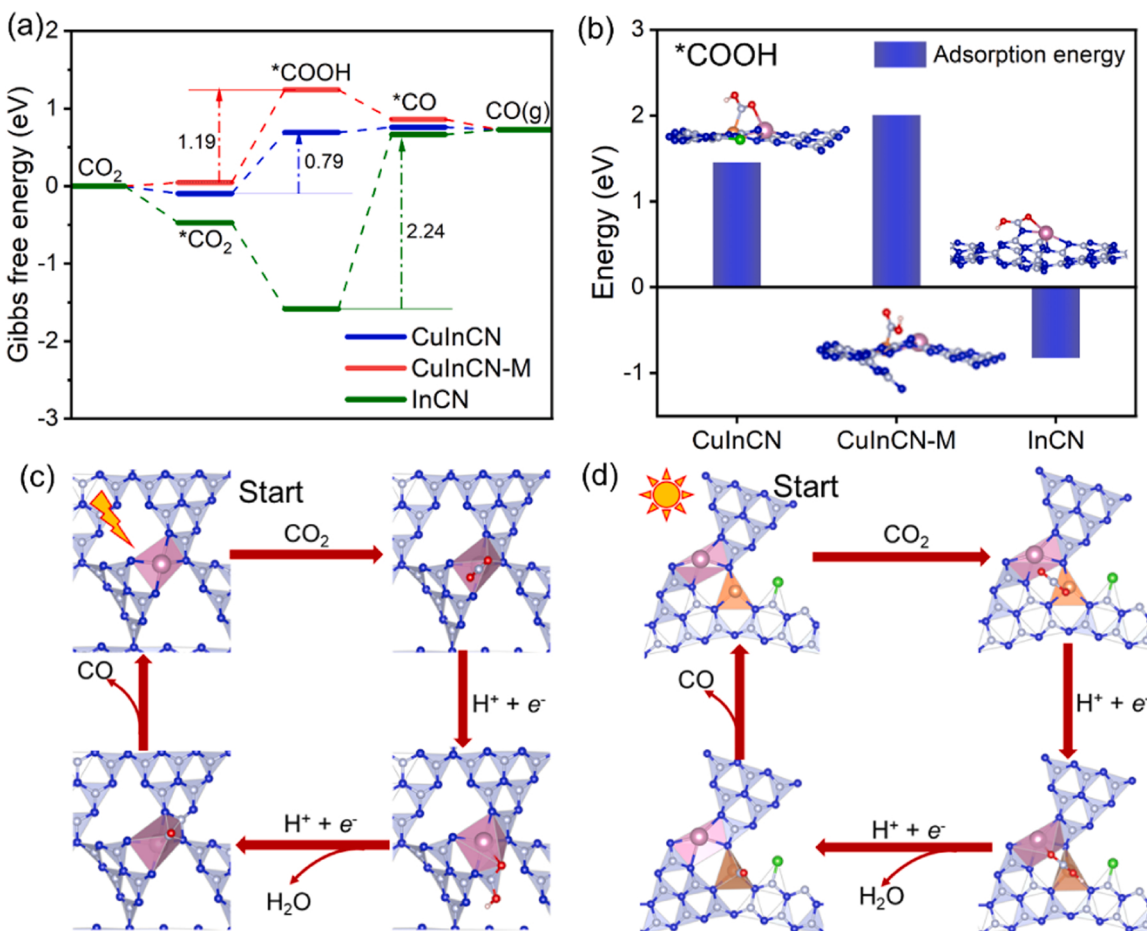


Fig. 6. Gibbs free energy diagrams of CO₂ photoreduction to CO (a), the adsorption model and adsorption energy of *COOH on CuInCN, CuInCN-M and InCN (b). Photocatalytic mechanism on InCN (c), CuInCN (d). (light gray: C atom, blue: N atom, red: O atom, dusty pink: H atom, pale purple: In atom, orange: Cu atom, green: Cl atom).

Cu-C binding on CuInCN. By contrast, $^{*}\text{COOH}$ is only adsorbed only on Cu sites by Cu-C binding on CuInCN without Cl model. For InCN, except In site, one of the neighboring N atoms is also attributed to $^{*}\text{COOH}$ adsorption by N-C binding. As a result, adsorption energy of $^{*}\text{COOH}$ on InCN is the lowest among these three catalysts, indicating that $^{*}\text{COOH}$ on InCN is most stable. It also means that it is not easy for $^{*}\text{COOH}$ to dissociate on InCN. CuInCN shows a moderate $^{*}\text{COOH}$ adsorption, not too strong like InCN, nor too weak like CuInCN-M. Therefore, it is beneficial for the $^{*}\text{COOH}$ formation and transformation on CuInCN. The $^{*}\text{COOH}$ adsorption difference on the three catalysts is related to the electronic structure of In sites. Because there is a strong charge depletion on In site in InCN, In site binds with O of $^{*}\text{COOH}$ much stronger, $^{*}\text{COOH}$ is difficult to dissociate to form $^{*}\text{CO}$, which is the reason why $^{*}\text{COOH} \rightarrow ^{*}\text{CO}$ is the rate-determining step on InCN. In site does not participate in $^{*}\text{COOH}$ adsorption due to the weak positive charge of In sites in CuInCN-M. However, for CuInCN, the electronic property of In and Cu atoms are modulated by Cl atom, which makes the electronegativity of the In and Cu sites moderate. It comes out that In and Cu dual sites participate in $^{*}\text{COOH}$ adsorption to lower energy barrier of $^{*}\text{COOH}$ formation.

Taking into considerations of the experimental and DFT calculation results and analysis, the mechanism of CO_2 photoreduction to CO on InCN and CuInCN is proposed as schematically depicted in Fig. 6c,d. The photoexcited catalyst generates the electrons and holes. TEOA acts as the hole scavenger. And the electrons on catalysts transfer to homogeneous $[\text{Co}(\text{bpy})_3]^{2+}$, which functions as cocatalyst to accelerate the electron transfer processes. On InCN, adsorbed CO_2 combined with one electron and proton to form $^{*}\text{COOH}$ on In and its neighboring N site. Then, $^{*}\text{COOH}$ obtained one electron and proton dissociates to form $^{*}\text{CO}$ and H_2O . The adsorbed $^{*}\text{CO}$ on In site finally desorbs to produce CO gas. On CuInCN, the $^{*}\text{COOH}$ formed is adsorbed on Cu and In dual sites when CO_2 reacts with one electron and proton. Then, the next step of $^{*}\text{CO}$ formed by $^{*}\text{COOH}$ dissociation occurs on Cu site. Finally, $^{*}\text{CO}$ desorbs to form CO product.

4. Conclusion

In summary, an atomically dispersed photocatalyst consisting of Cl atom tailored p-d blocks In-Cu dual metal anchored on polymeric carbon nitride was prepared by a facile thermal polymerization approach for photocatalytic CO_2 RR. The work shows that this CuInCN catalyst has an outstanding catalytic activity for CO_2 photoconversion to CO. Experimental investigation coupled with DFT calculations unveil the in-depth mechanism to underpin the high performance. Firstly, the introduction of d-block Cu atoms into InCN enhances the light absorption, increases the electronic conductivity, promotes the charge separation by accelerating the charge transfer from CN to metal sites, provides the catalytic active sites. Subsequently, Cl atom in the structure further promotes charge separation and electron mobility, modulates the electronic structure of In and Cu sites to make them synergistically interact with $^{*}\text{COOH}$. Finally, these make CuInCN collectively lower the activation energy of reaction.

CRediT authorship contribution statement

Hainan Shi: Conceptualization, Data curation, Formal analysis, Investigation, Writing – review & editing, Writing – original draft. **Jiahui Li:** Investigation, Formal analysis, Resources, Data curation. **Haozhi Wang:** Methodology, Data curation, Formal analysis. **Jungang Hou:** Supervision, Project administration, Funding acquisition, Writing – review & editing. **Keyan Li:** Supervision, Project administration. **Xinwen Guo:** Supervision, Project administration, Funding acquisition, Writing – review & editing.

Declaration of Competing Interest

All authors declare that they have no known competing financial interests or personal relationships that could have appeared to influence the work reported in this paper.

Data availability

Data will be made available on request.

Acknowledgments

This work was supported by National Natural Science Foundation of China (21972015, 22088102, 22278056), Young Top Talents Project of Liaoning Province (XLYC1907147), Joint Research Fund Liaoning-Shenyang National Laboratory for Materials Science (2019JH3/30100003), the Fundamental Research Funds for the Central Universities (DUT20TD06, DUT22LAB602) and the Liaoning Revitalization Talent Program (XLYC2008032). Hainan Shi and Jiahui Li contributed equally to this work.

Appendix A. Supplementary material

Supplementary data associated with this article can be found in the online version at doi:10.1016/j.apcatb.2022.122139.

References

- [1] R. Schäppi, D. Rutz, F. Dähler, A. Muroyama, P. Haueter, J. Lilliestam, A. Patt, P. Furler, A. Steinfeld, Drop-in fuels from sunlight and air, *Nature* 601 (2021) 63–68.
- [2] A. Wagner, C.D. Sahm, E. Reisner, Towards molecular understanding of local chemical environment effects in electro- and photocatalytic CO_2 reduction, *Nat. Catal.* 3 (2020) 775–786.
- [3] H. Lin, S. Luo, H. Zhang, J. Ye, Toward solar-driven carbon recycling, *Joule* 6 (2022) 294–314.
- [4] S. Wang, X. Han, Y. Zhang, N. Tian, T. Ma, H. Huang, Inside-and-out semiconductor engineering for CO_2 photoreduction: from recent advances to new trends, *Small Struct.* 2 (2021) 2000061.
- [5] F. Jiao, J. Li, X. Pan, J. Xiao, H. Li, H. Ma, M. Wei, Y. Pan, Z. Zhou, M. Li, S. Miao, J. Li, Y. Zhu, D. Xiao, T. He, J. Yang, F. Qi, Q. Fu, X. Bao, Selective conversion of syngas to light olefins, *Science* 351 (2016) 1065–1068.
- [6] J. Li, Y. He, L. Tan, P. Zhang, X. Peng, A. Oruganti, G. Yang, H. Abe, Y. Wang, N. Tsubaki, Integrated tuneable synthesis of liquid fuels via Fischer-Tropsch technology, *Nat. Catal.* 1 (2018) 787–793.
- [7] G. Chen, G.I.N. Waterhouse, R. Shi, J. Zhao, Z. Li, L.-Z. Wu, C.-H. Tung, T. Zhang, From solar energy to fuels: recent advances in light-driven C1 chemistry, *Angew. Chem. Int. Ed.* 58 (2019) 17528–17551.
- [8] C. Wang, W. Fang, Z. Liu, L. Wang, Z. Liao, Y. Yang, H. Li, L. Liu, H. Zhou, X. Qin, S. Xu, X. Chu, Y. Wang, A. Zheng, F.-S. Xiao, Fischer-Tropsch synthesis to olefins boosted by MFI zeolite nanosheets, *Nat. Nanotechnol.* (2022) 714–720.
- [9] G. Malta, A. Kondrat Simon, J. Freakley Simon, J. Davies Catherine, L. Lu, S. Dawson, A. Thethford, K. Gibson Emma, J. Morgan David, W. Jones, P. Wells Peter, P. Johnston, C.R.A. Catlow, J. Kiely Christopher, J. Hutchings Graham, Identification of single-site gold catalysis in acetylene hydrochlorination, *Science* 355 (2017) 1399–1403.
- [10] J. Mao, C.-T. He, J. Pei, W. Chen, D. He, Y. He, Z. Zhuang, C. Chen, Q. Peng, D. Wang, Y. Li, Accelerating water dissociation kinetics by isolating cobalt atoms into ruthenium lattice, *Nat. Commun.* 9 (2018) 4958–4965.
- [11] J. Gu, C.-S. Hsu, L. Bai, M. Chen Hao, X. Hu, Atomically dispersed Fe^{3+} sites catalyze efficient CO_2 electroreduction to CO, *Science* 364 (2019) 1091–1094.
- [12] H. Yang, Y. Wu, G. Li, Q. Lin, Q. Hu, Q. Zhang, J. Liu, C. He, Scalable production of efficient single-atom copper decorated carbon membranes for CO_2 electroreduction to methanol, *J. Am. Chem. Soc.* 141 (2019) 12717–12723.
- [13] Y. Zhao, H. Zhou, X. Zhu, Y. Qu, C. Xiong, Z. Xue, Q. Zhang, X. Liu, F. Zhou, X. Mou, W. Wang, M. Chen, Y. Xiong, X. Lin, Y. Lin, W. Chen, H.-J. Wang, Z. Jiang, L. Zheng, T. Yao, J. Dong, S. Wei, W. Huang, L. Gu, J. Luo, Y. Li, Y. Wu, Simultaneous oxidative and reductive reactions in one system by atomic design, *Nat. Catal.* 4 (2021) 134–143.
- [14] Y. Wu, Y. Zhao, P. Zhai, C. Wang, J. Gao, L. Sun, J. Hou, Triggering lattice oxygen activation of single-atomic Mo sites anchored on Ni-Fe oxyhydroxides nanoarrays for electrochemical water oxidation, *Adv. Mater.* 34 (2022) 2202523.
- [15] P. Zhai, M. Xia, Y. Wu, G. Zhang, J. Gao, B. Zhang, S. Cao, Y. Zhang, Z. Li, Z. Fan, C. Wang, X. Zhang, J.T. Miller, L. Sun, J. Hou, Engineering single-atomic ruthenium catalytic sites on defective nickel-iron layered double hydroxide for overall water splitting, *Nat. Commun.* 12 (2021) 4587–4597.

- [16] W. Zhong, R. Sa, L. Li, Y. He, L. Li, J. Bi, Z. Zhuang, Y. Yu, Z. Zou, A covalent organic framework bearing single Ni sites as a synergistic photocatalyst for selective photoreduction of CO₂ to CO, *J. Am. Chem. Soc.* 141 (2019) 7615–7621.
- [17] Y. Li, S. Wang, X. Wang, Y. He, Q. Wang, Y. Li, M. Li, G. Yang, J. Yi, H. Lin, D. Huang, L. Li, H. Chen, J. Ye, Facile top-down strategy for direct metal atomization and coordination achieving a high turnover number in CO₂ photoreduction, *J. Am. Chem. Soc.* 142 (2020) 19259–19267.
- [18] Y. Hu, F. Zhan, Q. Wang, Y. Sun, C. Yu, X. Zhao, H. Wang, R. Long, G. Zhang, C. Gao, W. Zhang, J. Jiang, Y. Tao, Y. Xiong, Tracking mechanistic pathway of photocatalytic CO₂ reaction at Ni sites using operando, time-resolved spectroscopy, *J. Am. Chem. Soc.* 142 (2020) 5618–5626.
- [19] H. Zhang, Y. Wang, S. Zuo, W. Zhou, J. Zhang, X.W.D. Lou, Isolated cobalt centers on W₁₈O₄₉ nanowires perform as a reaction switch for efficient CO₂ photoreduction, *J. Am. Chem. Soc.* 143 (2021) 2173–2177.
- [20] Y. Li, B. Li, D. Zhang, L. Cheng, Q. Xiang, Crystalline carbon nitride supported copper single atoms for photocatalytic CO₂ reduction with nearly 100% CO selectivity, *ACS Nano* 14 (2020) 10552–10561.
- [21] X. Xiong, C. Mao, Z. Yang, Q. Zhang, G.I.N. Waterhouse, L. Gu, T. Zhang, Photocatalytic CO₂ reduction to CO over Ni single atoms supported on defect-rich zirconia, *Adv. Energy Mater.* 10 (2020) 2002928.
- [22] Y. Chen, S. Ji, C. Chen, Q. Peng, D. Wang, Y. Li, Single-atom catalysts: synthetic strategies and electrochemical applications, *Joule* 2 (2018) 1242–1264.
- [23] K. Jiang, S. Siahrostami, T. Zheng, Y. Hu, S. Hwang, E. Stavitski, Y. Peng, J. Dynes, M. Gangisetty, D. Su, K. Attenkofer, H. Wang, Isolated Ni single atoms in graphene nanosheets for high-performance CO₂ reduction, *Energy Environ. Sci.* 11 (2018) 893–903.
- [24] X. Jin, R. Wang, L. Zhang, R. Si, M. Shen, M. Wang, J. Tian, J. Shi, Electron configuration modulation of nickel single atoms for elevated photocatalytic hydrogen evolution, *Angew. Chem. Int. Ed.* 59 (2020) 6827–6831.
- [25] S. Li, X. Lu, S. Zhao, M. Ceccato, X.-M. Hu, A. Roldan, M. Liu, K. Daasbjerg, p-block indium single-atom catalyst with low-coordinated In–N motif for enhanced electrochemical CO₂ reduction, *ACS Catal.* 12 (2022) 7386–7395.
- [26] H. Shang, T. Wang, J. Pei, Z. Jiang, D. Zhou, Y. Wang, H. Li, J. Dong, Z. Zhuang, W. Chen, D. Wang, J. Zhang, Y. Li, Design of a single-atom indium δ^{+} –N₄ interface for efficient electroreduction of CO₂ to formate, *Angew. Chem. Int. Ed.* 59 (2020) 22465–22469.
- [27] P. Lu, X. Tan, H. Zhao, Q. Xiang, K. Liu, X. Zhao, X. Yin, X. Li, X. Hai, S. Xi, A.T. S. Wee, S.J. Pennycook, X. Yu, M. Yuan, J. Wu, G. Zhang, S.C. Smith, Z. Yin, Atomically dispersed indium sites for selective CO₂ electroreduction to formic acid, *ACS Nano* 15 (2021) 5671–5678.
- [28] W. Guo, X. Tan, J. Bi, L. Xu, D. Yang, C. Chen, Q. Zhu, J. Ma, A. Tayal, J. Ma, Y. Huang, X. Sun, S. Liu, B. Han, Atomic indium catalysts for switching CO₂ electroreduction products from formate to CO, *J. Am. Chem. Soc.* 143 (2021) 6877–6885.
- [29] J. Wang, E. Kim, D.P. Kumar, A.P. Rangappa, Y. Kim, Y. Zhang, T.K. Kim, Highly durable and fully dispersed cobalt diatomic site catalysts for CO₂ photoreduction to CH₄, *Angew. Chem. Int. Ed.* 61 (2022), e202113044.
- [30] J. Gu, M. Jian, L. Huang, Z. Sun, A. Li, Y. Pan, J. Yang, W. Wen, W. Zhou, Y. Lin, H.-J. Wang, X. Liu, L. Wang, X. Shi, X. Huang, L. Cao, S. Chen, X. Zheng, H. Pan, J. Zhu, S. Wei, W.-X. Li, J. Lu, Synergizing metal–support interactions and spatial confinement boosts dynamics of atomic nickel for hydrogens, *Nat. Nanotechnol.* 16 (2021) 1141–1149.
- [31] C. Wang, K. Wang, Y. Feng, C. Li, X. Zhou, L. Gan, Y. Feng, H. Zhou, B. Zhang, X. Qu, H. Li, J. Li, A. Li, Y. Sun, S. Zhang, G. Yang, Y. Guo, S. Yang, T. Zhou, F. Dong, K. Zheng, L. Wang, J. Huang, Z. Zhang, X. Han, Co and Pt dual-single-atoms with oxygen-coordinated Co–O–Pt dimer sites for ultrahigh photocatalytic hydrogen evolution efficiency, *Adv. Mater.* 33 (2021) 2003327.
- [32] L. Cheng, X. Yue, L. Wang, D. Zhang, P. Zhang, J. Fan, Q. Xiang, Dual-single-atom tailoring with bifunctional integration for high-performance CO₂ photoreduction, *Adv. Mater.* 33 (2021) 2105135–2105145.
- [33] N. Zhang, X. Zhang, Y. Kang, C. Ye, R. Jin, H. Yan, R. Lin, J. Yang, Q. Xu, Y. Wang, Q. Zhang, L. Gu, L. Liu, W. Song, J. Liu, D. Wang, Y. Li, A supported Pd₂ dual-atom site catalyst for efficient electrochemical CO₂ reduction, *Angew. Chem. Int. Ed.* 60 (2021) 13388–13393.
- [34] B. Zhang, J. Zhang, J. Shi, D. Tan, L. Liu, F. Zhang, C. Lu, Z. Su, X. Tan, X. Cheng, B. Han, L. Zheng, J. Zhang, Manganese acting as a high-performance heterogeneous electrocatalyst in carbon dioxide reduction, *Nat. Commun.* 10 (2019) 2980–2987.
- [35] F. Xu, K. Meng, B. Cheng, S. Wang, J. Xu, J. Yu, Unique S-scheme heterojunctions in self-assembled TiO₂/CsPbBr₃ hybrids for CO₂ photoreduction, *Nat. Commun.* 11 (2020) 4613–4621.
- [36] S. Liu, C. Li, M.J. Zachman, Y. Zeng, H. Yu, B. Li, M. Wang, J. Braaten, J. Liu, H. M. Meyer, M. Lucero, A.J. Kropf, E.E. Alp, Q. Gong, Q. Shi, Z. Feng, H. Xu, G. Wang, D.J. Myers, J. Xie, D.A. Cullen, S. Litster, G. Wu, Atomically dispersed iron sites with a nitrogen–carbon coating as highly active and durable oxygen reduction catalysts for fuel cells, *Nat. Energy* 7 (2022) 652–663.
- [37] L. Liu, H. Huang, Z. Chen, H. Yu, K. Wang, J. Huang, H. Yu, Y. Zhang, Synergistic polarization engineering on bulk and surface for boosting CO₂ photoreduction, *Angew. Chem. Int. Ed.* 60 (2021) 18303–18308.